Time-dependent wave splitting and source separation

M. J. Grote, M. Kray, F. Nataf, F. Assous

Time-dependent wave splitting and source separation

Marcus J. Grote[a], Marie Kray[a], Frédéric Nataf[b,c,d], Franck Assous[e]

[a] Department of Mathematics and Computer Science, University of Basel, Spiegelgasse 1, CH-4051 Basel, Switzerland, {marcus.grote,marie.kray}@unibas.ch
[b] CNRS, UMR 7598, Laboratoire Jacques-Louis Lions, F-75005, Paris, France
[c] UPMC Univ Paris 06, UMR 7598, Laboratoire Jacques-Louis Lions, F-75005, Paris, France, nataf@ann.jussieu.fr
[d] INRIA Rocquencourt, Alpines, BP 105, 78153 Le Chesnay Cedex, France
[e] Department of Mathematics, Ariel University, 40700, Ariel, Israel, franckassous55@gmail.com

Abstract

Starting from classical absorbing boundary conditions, we propose a method for the separation of time-dependent scattered wave fields due to multiple sources or obstacles. In contrast to previous techniques, our method is local in space and time, deterministic, and also avoids *a priori* assumptions on the frequency spectrum of the signal. Numerical examples in two space dimensions illustrate the usefulness of wave splitting for time-dependent scattering problems.

1. Introduction

As natural information carriers, acoustic, electromagnetic and elastic waves are ubiquitous for probing an unknown medium to determine its internal geometric or material properties. When the incident probing wave encounters an inhomogeneity, it generates a scattered wave which carries information about the obstacle across the background medium. From that scattering data, usually recorded at remote sensors, the nature, location and shape of the obstacle buried inside the medium can be recovered, as in seismic full waveform inversion, medical imaging, and nondestructive testing. Clearly, that information is readily available by subtraction of the incident

wave from total field measurements. However, if the location, spatial distribution or time dependence of the original source are not precisely known, or other undesired sources interfere with the signal, extraction of the scattered field of interest becomes non-trivial, though it remains essential for any subsequent inversion.

Blind source separation in signal processing [6], for instance, attempts to separate the input signals from their recorded mixture, much like in the well-known "cocktail-party effect" where listeners perceptually focus on a single target voice against competing sound sources. Ray-based in nature, blind source separation uses statistical tools to detect individual sources [8] or remove noise [2] from linearly superimposed signals.

In transcranial ultrasonic imaging, intense ultrasound pulses induce a single cavitation bubble whose collapse generates a small shock wave then recorded by a standard ultrasound imaging array [22]; clearly, the bubble's time signature is never precisely known. Similarly, the detection of individual free-floating and targeted microbubbles of an ultrasound contrast agent is critical for quantifying the amount of bubbles in the tissue [20]. Yet another application is photoacoustic imaging, where laser pulses are delivered into biological tissues thereby leading to transient thermoelastic expansion and subsequent ultrasonic emission. Again, the quantity of interest is the time signature of the laser induced pressure wave generated by an unknown source [25].

When two or more obstacles are present, each primary scattered wave will induce secondary scattered waves from all other obstacles, which again will induce further scattered waves, and so forth. Together with the incident wave, their superposition results in the measured total wave field. The inversion from the total wave field for multiple obstacles at once adds yet another layer of complexity to any algorithm for inverse scattering problems. Hence, if their superposition can be split into individual outgoing components, we can apply any algorithm for single inverse scattering to each scatterer separately. As a consequence, each isolated scattering problem will be smaller in size and less ill-conditioned than their total sum.

In seismic imaging, for instance, shear-wave splitting has been successfully used for earthquake prediction or in the petroleum industry. Indeed when a polarized elastic shear wave enters a new, anisotropic medium, it splits into two shear waves whose mutual time-delay and orientation then allows to infer the density and orientation of the cracks in the medium. In [21], Kreider uses Weston's theoretical wave splitting for stratified media [27] to reconstruct

the unknown velocity function in a stratified inhomogeneous cylinder from reflection data.

There is a long history of wave splitting techniques for multiple scattering problems, especially in the frequency domain. In his classical work, Twerksy expresses multiple scattering coefficients in terms of algebraic relations which couple the multipole coefficients of isolated scatterers – see [26] for a review. More recently, Grote and Kirsch [12] used wave splitting to derive nonreflecting boundary conditions for multiple scattering problems. Similarly, Acosta [1] formulated on-surface radiation conditions for multiple scattering. In [7], Ben Hassen, Liu and Potthast split the far-field pattern using integral based formulations to extend the point source method to inverse scattering of multiple obstacles. By combining the inverse Radon approximation with a Galerkin ansatz, Griesmaier, Hanke and Sylvester determine the convex scattering support of individual far-field components separately [10].

In the time domain, little work on inverse multiple scattering problems is available. In [13, 15], nonreflecting boundary conditions for time-dependent multiple scattering were derived, which avoid the space-time integrals involved in standard integral-based formulations. By Fourier transform in the frequency domain, Potthast, Fazi and Nelson [23] devised a filter via the point source method for time-dependent source separation.

Here we propose a method to determine the separate outgoing components of the incident and scattered wave fields for time-dependent scattering problems. In contrast to previous work, our approach is local in space and time, deterministic, and also avoids any *a priori* assumptions on the frequency spectrum of the signal. Starting from the standard Bayliss-Turkel [5] absorbing boundary conditions, we present in Section 2 the principle of wave splitting, first introduced in [14], which we then illustrate in the simpler one-dimensional case. Next, in Section 3, we present our wave splitting approach in the general two-dimensional case and also discuss its numerical implementation. Finally, in Section 4, we consider two distinct numerical experiments to illustrate the usefulness of our wave splitting approach.

2. Wave splitting

We consider wave scattering from two distinct scatterers, which each may contain several obstacles, inhomogeneities and nonlinearity. Both scatterers are well separated, that is we assume that we can surround them by two non-intersecting spheres S_1 and S_2 centered at C_1 and C_2, respectively –

see Fig. 1. In Ω, the unbounded domain outside S_1 and S_2, the scattered wave field u satisfies:

$$\frac{\partial^2 u}{\partial t^2} - c^2 \Delta u = 0 \qquad \text{in } \Omega, \quad t > 0, \tag{1}$$

with constant wave speed $c > 0$. Moreover, we assume that u is initially confined to the interior of $S_1 \cup S_2$; thus, it is zero throughout Ω at time $t = 0$. Then u splits into two unique wave fields u_1 and u_2 as

$$u = u_1 + u_2 \qquad \text{in } \Omega, \quad t > 0, \tag{2}$$

where each u_k is purely outgoing and satisfies (1) in the entire exterior of S_k [13]; hence, u_k is determined by its time-dependent (unknown) values on S_k, $k = 1, 2$.

Since each u_k is outgoing outside S_k, it can be written as a progressive wave expansion in inverse powers of distance [5, 16] from C_k. In three space dimensions, for instance, we have

$$u_k(t, r_k, \theta_k, \varphi_k) = \frac{1}{r_k} \sum_{i \geq 0} \frac{f_{k,i}(r_k - ct, \theta_k, \varphi_k)}{(r_k)^i}, \tag{3}$$

where $(r_k, \theta_k, \varphi_k)$ denote spherical coordinates centered about the origin C_k, $k = 1, 2$. In two space dimensions, the progressive wave expansion of u_k converges only asymptotically:

$$u_k(t, r_k, \theta_k) \sim \frac{1}{\sqrt{r_k}} \sum_{i \geq 0} \frac{f_{k,i}(r_k - ct, \theta_k)}{(r_k)^i}, \qquad r_k \to \infty, \tag{4}$$

where (r_k, θ_k) denote polar coordinates centered about the origin C_k, $k = 1, 2$.

Starting from (3), (4) respectively, Bayliss and Turkel [5] derived a sequence of increasingly accurate differential operators of order m that annihilate the m leading order terms in either expansion above for $k = 1, 2$:

$$B_k^m[u_k] := \prod_{\ell=1}^{m} \left(\frac{1}{c} \frac{\partial}{\partial t} + \frac{\partial}{\partial r_k} + \frac{2\ell - 1}{r_k} \right) = O\left(\frac{1}{r_k^{2m+1}} \right), \quad \Omega \subset \mathbb{R}^3, \tag{5}$$

$$B_k^m[u_k] := \prod_{\ell=1}^{m} \left(\frac{1}{c} \frac{\partial}{\partial t} + \frac{\partial}{\partial r_k} + \frac{4\ell - 3}{2r_k} \right) = O\left(\frac{1}{r_k^{2m+\frac{1}{2}}} \right), \quad \Omega \subset \mathbb{R}^2. \tag{6}$$
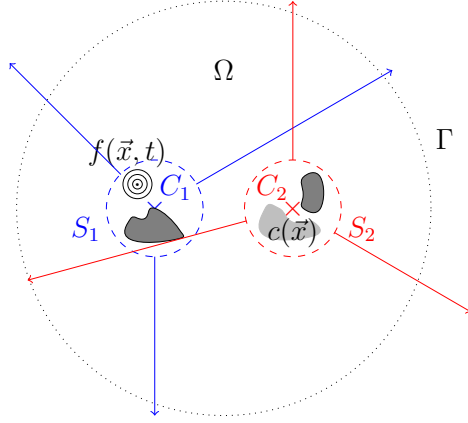
4

Figure 1: Two distinct scatterers and their corresponding outgoing wave fields.

By setting

$$B_k^m[u_k] \;=\; 0, \tag{7}$$

each operator yields an absorbing boundary condition on any (convex) surface patch in three dimensions or curve segment in two dimensions.

Now, let Γ denote a surface patch or curve segment, not necessarily closed or connected, which lies inside Ω. Neglecting the error term in (5)-(6), we thus obtain on Γ

$$B_j^m[u_k] \;=\; B_j^m[u_k + u_j] = \; B_j^m[u], \qquad j = 1, 2, \quad k \neq j. \tag{8}$$

When u is known on Γ, equation (8) yields a partial differential equation for the unknown wave field u_k. In general, it will involve tangential, normal and time derivatives. To restrict (8) to Γ, we rewrite the normal derivative (∂_{r_j}) as a combination of tangential and radial (∂_{r_k} and ∂_{θ_k}) derivatives and then replace radial by time derivatives using (3) or (4), respectively. The resulting equation will involve only tangential and time derivatives and thus be restricted to Γ. Clearly, appropriate initial and boundary conditions must be set on Γ for well-posedness. In fact, since the scattered field is initially zero in Ω, both u_k and u_j vanish on Γ at $t = 0$.

Remark 2.1. *In (8), the absorbing differential operator B_j^m enables the recovery of every outgoing component of the total field into Ω in forward time. Instead, we can also consider time-reversed wave fields propagating backwards*

5

in time. By replacing the coupled space-time variable $r_k - ct$ by $r_k + ct$ in the progressive wave expansions (3),(4), we thus obtain differential operators which instead annihilate incoming wave fields.

In the three-dimensional case, for instance, let $B_j = B_j^1$ denote the first-order Bayliss-Turkel operator:

$$B_j[u] = \left(\frac{1}{c} \frac{\partial}{\partial t} + \frac{\partial}{\partial r_j} + \frac{1}{r_j} \right) u. \tag{9}$$

Then, the new operator for the time-reversed total field, u_R, reads:

$$B_{R,j}[u_R] = \left(\frac{1}{c} \frac{\partial}{\partial t} - \frac{\partial}{\partial r_j} - \frac{1}{r_j} \right) u_R. \tag{10}$$

Thus, it is possible to extend wave-splitting even to parts of Γ, where the forward problem (8) may be ill-posed. To use this time reversed operator, however, we must also set an initial condition for $u_{R,k}$ or $u_{R,j}$ at the final time $t = T$. If T is sufficiently large so that the total wave field has entirely left Ω, we can simply set $u_{R,k}$ and $u_{R,j}$ to zero at time $t = T$ as initial condition for wave splitting in time reversal. ∎

2.1. One-dimensional wave splitting

Before proceeding with the higher dimensional case, we briefly consider the much simpler one-dimensional situation to illustrate the basic principle of wave splitting. Hence we consider two sources located inside of two disjoint intervals S_1 and S_2, separated by an interval Ω_I – see Fig. 2. Now, as waves are excited inside S_1 and S_2, they propagate into Ω_I where they mingle and form the total wave field $u(t, x)$. Since u is initially zero and the wave speed, c, is assumed constant outside the two scatterers, the total field consists of a right-moving wave, u_1, and a left-moving wave, u_2:

$$u(t, x) = u_1(x - c\,t) + u_2(x + c\,t), \qquad x \in \Omega_I, t \geq 0. \tag{11}$$

Next, let x_Γ denote an observation point located well inside Ω_I. Given the time history of the total field $u(t, x_\Gamma)$ at the receiver, we wish to recover the two individual one-way wave fields u_1 and u_2.

Following the approach delineated in the previous section for the two- or three-dimensional case, we consider the one-way differential operators

$$B_1[u] \;:=\; \frac{\partial u}{\partial t} + c\,\frac{\partial u}{\partial x}, \qquad B_2[u] \;:=\; \frac{\partial u}{\partial t} - c\,\frac{\partial u}{\partial x}. \tag{12}$$
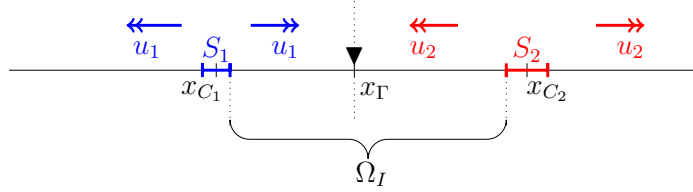
6

Figure 2: One-dimensional wave splitting. The receiver is located at x_Γ.

Since $B_1[u_1] = B_2[u_2] = 0$, we thus obtain the one-dimensional counterpart of (8) inside Ω_I:

$$B_1[u_2] = B_1[u_1] + B_1[u_2] = B_1[u], \tag{13}$$
$$B_2[u_1] = B_2[u_1] + B_2[u_2] = B_2[u]. \tag{14}$$

Hence, equations (13),(14) correspond to partial differential equations for the unknown wave fields u_1, u_2 which both involve derivatives in space and time. Since $B_2[u_2] = 0$ inside Ω_I, we can replace in (13) the space by the time derivative of u_2, and similarly for u_1 in (14):

$$B_1[u_2] = \frac{\partial u_2}{\partial t} + c\frac{\partial u_2}{\partial x} = 2\frac{\partial u_2}{\partial t},$$
$$B_2[u_1] = \frac{\partial u_1}{\partial t} - c\frac{\partial u_1}{\partial x} = 2\frac{\partial u_1}{\partial t}.$$

Setting $x = x_\Gamma$ in the resulting equations, we obtain the two ordinary equations:

$$\frac{\partial u_2}{\partial t}(x_\Gamma + c\,t) = \frac{1}{2} B_1[u](t, x_\Gamma), \tag{15}$$
$$\frac{\partial u_1}{\partial t}(x_\Gamma - c\,t) = \frac{1}{2} B_2[u](t, x_\Gamma). \tag{16}$$

To recover u_1 or u_2, we shall integrate (15) and (16) in time, together with homogeneous initial conditions, since the signal at x_Γ is initially zero. Here, we opt for the Crank-Nicolson scheme and let $u_2^n \simeq u_2(x_\Gamma + c\,t^n)$, $u_1^n \simeq u_1(x_\Gamma - c\,t^n)$ denote the numerical approximations at time $t^n = n\Delta t$, $\Delta t > 0$. The discrete time-marching scheme then reads:

$$u_2^{n+1} = u_2^n + \frac{\Delta t}{4}\left(B_1[u](t^{n+1}, x_\Gamma) + B_1[u](t^n, x_\Gamma)\right), \quad n \geq 0, \tag{17}$$

$$u_1^{n+1} = u_1^n + \frac{\Delta t}{4}\left(B_2[u](t^{n+1}, x_\Gamma) + B_2[u](t^n, x_\Gamma)\right), \quad n \geq 0, \tag{18}$$
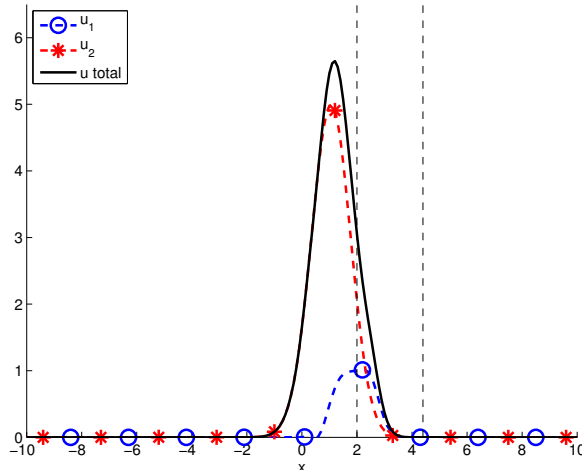
7

Figure 3: One-dimensional wave splitting. Snapshot of the total field u with the right- and left-propagating waves u_1 and u_2 at time $t = 7.45$. The two receivers are located at $x_\Gamma = 2$ and $x_\Gamma = 4.4$ (vertical dashed lines).

and $u_2^0 = 0$, $u_1^0 = 0$. The right-hand-side is discretized using centered finite differences in time and in space in our simulation, assuming we know u in a small neighborhood of x_Γ.

For illustration, we consider a numerical experiment with $c = 1$ and the two intervals $S_1 = [-8, -3]$, $S_2 = [5, 12]$ centered about $x_{C_1} = -5.5$, $x_{C_2} = 8.5$, respectively. Inside each interval, we initialize a Gaussian-like wave

$$u_1(x, t) = e^{-((x - x_{C_1}) - ct)^4} \chi_{S_1}(x), \qquad u_2(x, t) = 5 e^{-((x - x_{C_2}) + ct)^2} \chi_{S_2}(x),$$

where χ_S denotes the characteristic function of S. Hence the total field,

$$u(x, t) = e^{-((x - x_{C_1}) - ct)^4} \chi_{S_1}(x) + 5 e^{-((x - x_{C_2}) + ct)^2} \chi_{S_2}(x),$$

is identically zero at $t = 0$ inside Ω_I.

In Fig. 3, we display a snapshot of the total field $u(t, x)$ at time $t = 7.45$ together with the right- and left-propagating waves u_1 and u_2 that we wish to recover. For the reconstruction of u_1 and u_2, we consider two distinct locations: $x_\Gamma = 2$ and $x_\Gamma = 4.4$. At $x_\Gamma = 4.4$, u_1 and u_2 can easily be separated because of their very different arrival times – see left column of Fig. 4.
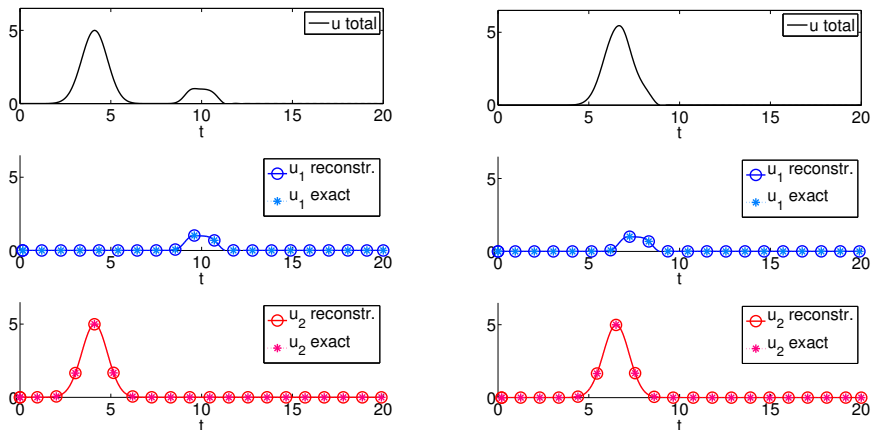
8

Figure 4: One-dimensional wave splitting. Reconstruction of the time history of u_1 and u_2 at $x_\Gamma = 4.4$ (left column) and $x_\Gamma = 2$ (right column) from the total field u using (18) and (17).

At $x_\Gamma = 2$, however, the two fields are completely superimposed and thus difficult to separate by eye-ball only – see right column of Fig. 4. In either case, our approach allows us to recover the full time history of u_1 and u_2 at the receiver's location with high accuracy.

For simplicity, here the considered wave speed c is constant everywhere; hence, the exact wave fields u_1, u_2 and u are readily available. Our wave splitting approach, however, also immediately applies to the situation when $c(x)$ varies inside S_1 and S_2.

3. Two-dimensional case

We shall now apply the wave splitting technique delineated in Section 2 to a typical two-dimensional configuration. Hence, we assume that the total field u is recorded on a circle Γ centered at either of the two sources C_1 or C_2. Given the measured values of u on Γ, here a circle centered about C_1 – see Fig. 5 – we shall recover both outgoing fields u_1 and u_2 using first-order absorbing differential operators.
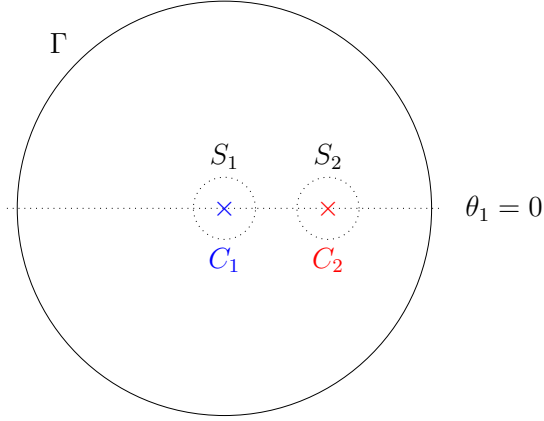
9

Figure 5: The two sources are located inside S_1 and S_2, while the measurements are located on the circle Γ, centered at C_1.

3.1. Recovery of u_1

First, we shall show how to recover u_1 on Γ from u. Let (r_k, θ_k) denote polar coordinates centered at C_k, $k = 1, 2$. Now, let the $\theta_1 = 0$ axis coincide with the line segment connecting C_1 and C_2, which is always possible by rotating the coordinate system. Following the derivation in Section 2, we apply $B_2 := B_2^1$ from (6) to the measured total field u, which yields the two-dimensional counterpart of (8):

$$\left(\frac{1}{c}\frac{\partial}{\partial t} + \frac{\partial}{\partial r_2} + \frac{1}{2r_2}\right)u_1 = \left(\frac{1}{c}\frac{\partial}{\partial t} + \frac{\partial}{\partial r_2} + \frac{1}{2r_2}\right)u. \tag{19}$$

To restrict equation (19) for u_1 to Γ, we first change coordinates and then replace any remaining normal by time derivatives using that $B_1[u_1] = 0$. More specifically, we use

$$\frac{\partial}{\partial r_2} = \frac{r_2 + \ell\cos(\theta_2)}{r_1}\frac{\partial}{\partial r_1} + \frac{\ell\sin(\theta_2)}{r_1^2}\frac{\partial}{\partial\theta_1} \tag{20}$$

$$\frac{\partial}{\partial r_1}(\sqrt{r_1}u_1) = -\frac{1}{c}\frac{\partial}{\partial t}(\sqrt{r_1}u_1), \tag{21}$$

with ℓ the distance between C_1 and C_2, to rewrite (19) for the leading order term $f_1 := f_{1,0}(r_1 - ct, \theta_1)$ of the series expansion in (4) as

$$\left(\alpha_1(\theta_1)\frac{\partial}{\partial t} + \beta_1(\theta_1)\frac{\partial}{\partial\theta_1} + \gamma_1(\theta_1)\right)f_1 = \left(\frac{1}{c}\frac{\partial}{\partial t} + \frac{\partial}{\partial r_2} + \frac{1}{2r_2}\right)u. \tag{22}$$

Here, the coefficient functions α_1, β_1 and γ_1 in (22) are given by

$$\alpha_1(\theta_1) \;=\; \frac{\sqrt{r_1^2 + \ell^2 - 2r_1\ell\cos(\theta_1)} - r_1 + \ell\cos(\theta_1)}{c\sqrt{r_1}\sqrt{r_1^2 + \ell^2 - 2r_1\ell\cos(\theta_1)}}, \tag{23}$$

$$\beta_1(\theta_1) \;=\; \frac{\ell\sin(\theta_1)}{r_1\sqrt{r_1}\sqrt{r_1^2 + \ell^2 - 2r_1\ell\cos(\theta_1)}}, \tag{24}$$

$$\gamma_1(\theta_1) \;=\; \frac{\ell\cos(\theta_1)}{2r_1\sqrt{r_1}\sqrt{r_1^2 + \ell^2 - 2r_1\ell\cos(\theta_1)}}. \tag{25}$$

Note that both ℓ and r_1 are constant on Γ, while

$$r_1^2 + \ell^2 - 2r_1\ell\cos(\theta_1) > 0, \qquad \forall\,\theta_1 \in [-\pi, \pi].$$

In (22), we have derived a partial differential equation for $f_1(r_1 - ct, \theta_1)$, which only involves time and space derivatives of f_1 tangential to Γ. To determine the domain of validity and the well-posedness of the hyperbolic equation (22), we now study the sign of each coefficient, which determines the directions of the characteristics and thus dictates the appropriate boundary conditions, if any, needed. As initial condition, we set u_1 to zero on Γ, as u is initially zero inside Ω.

Since

$$r_1^2 + \ell^2 - 2r_1\ell\cos(\theta_1) \geq r_1^2 + \ell^2\cos(\theta_1)^2 - 2r_1\ell\cos(\theta_1) = (r_1 - \ell\cos(\theta_1))^2,$$

we have

$$\sqrt{r_1^2 + \ell^2 - 2r_1\ell\cos(\theta_1)} \;\geq\; r_1 - \ell\cos(\theta_1).$$

Therefore, $\alpha_1(\theta_1) \geq 0$ for all $\theta_1 \in [-\pi, \pi]$; note that $\alpha_1 = 0$ for $\theta_1 = 0, \pi$.

We now proceed likewise for β_1 and γ_1. Since ℓ and r_1 are positive, β_1 is nonnegative for $\theta_1 \in [0, \pi]$. For $\theta_1 = 0, \pi$, $\beta_1(\theta_1)$ vanishes and hence (22) reduces to a trivial equation (without derivatives) in time. In that sense, both $\theta_1 = 0, \pi$ are singular points. From (25), we infer that γ_1 is positive for $\theta_1 \in (-\pi/2, \pi/2)$, negative for $\theta_1 \in (\pi/2, 3\pi/2)$, and vanishes for $\theta_1 = -\pi/2, \pi/2$. Since (22) is unstable when the signs of γ_1 and α_1 do not match, and $\alpha_1(\theta_1) \geq 0$ for all θ_1, we conclude that (22) is stable only for $\theta_1 \in [-\pi/2, \pi/2]$ – see Fig. 8.
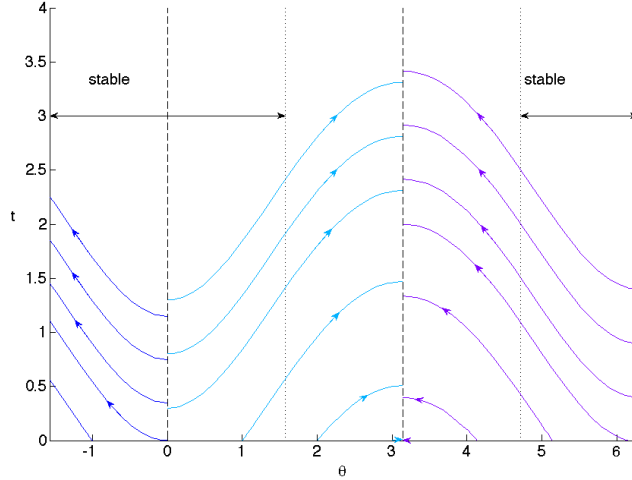
11

Figure 6: Characteristic curves for (22) starting from different angles θ

In Fig. 6, we display the characteristics of (22) and clearly observe two distinguished points: $\theta_1 = 0$ and $\theta_1 = \pi$. At $\theta_1 = 0$, the characteristics are always incoming and thus $\theta_1 = 0$ yields an appropriate initial condition to recover the signal in both intervals $[0, \pi)$ and $(-\pi, 0]$. On the contrary, $\theta_1 = \pi$ is never reached by any characteristic (except for that starting from $\theta = \pi$ itself). From these considerations, we impose at $\theta_1 = 0$ a Dirichlet boundary condition to solve (22) in a stable manner on the two independent quarter-circles $[0, \pi/2]$ and $[-\pi/2, 0]$.

To determine u_1 on the remaining half-circle, $\theta_1 \in [\pi/2, 3\pi/2]$, where u_1 is exponentially growing, we consider the time-reversed counterpart of (22). Hence, we let u_R denote the time-reversed total wave field and apply the time-reversed first-order Bayliss-Turkel operator $B_{R,2}$ – see Remark 2.1 – which yields:

$$\left(\frac{1}{c}\frac{\partial}{\partial t} - \frac{\partial}{\partial r_2} - \frac{1}{2r_2}\right) u_{R,1} = \left(\frac{1}{c}\frac{\partial}{\partial t} - \frac{\partial}{\partial r_2} - \frac{1}{2r_2}\right) u_R. \qquad (26)$$

Following the previous derivation (19)-(22), we replace the normal derivative by tangential and time derivatives in (26) using (20), (21). This yields the time-reversed counterpart of (22) for the leading term, $f_{R,1}$, in the series
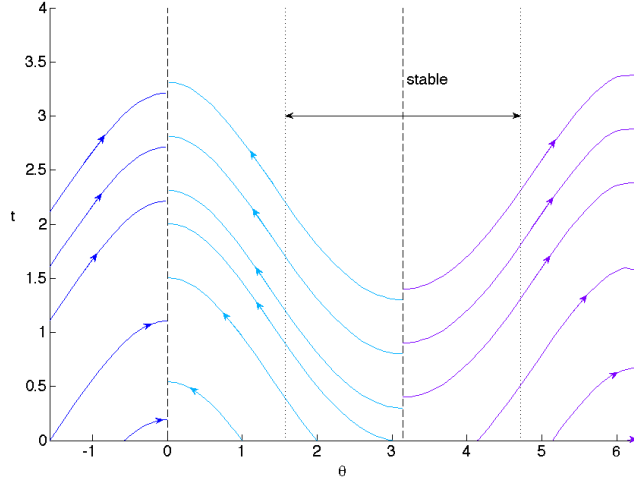
12

Figure 7: Characteristic curves for (27) starting from different angles θ

expansion of the time-reversed wave field:

$$\left(\alpha_{R,1}(\theta_1)\frac{\partial}{\partial t} + \beta_{R,1}(\theta_1)\frac{\partial}{\partial\theta_1} + \gamma_{R,1}(\theta_1)\right)f_{R,1} = \left(\frac{1}{c}\frac{\partial}{\partial t} - \frac{\partial}{\partial r_2} - \frac{1}{2r_2}\right)u_R. \tag{27}$$

Here, the coefficient functions are given by

$$\alpha_{R,1}(\theta_1) = \alpha_1(\theta_1), \qquad \beta_{R,1}(\theta_1) = -\beta_1(\theta_1), \qquad \gamma_{R,1}(\theta_1) = -\gamma_1(\theta_1), \tag{28}$$

with α_1, β_1 and γ_1 as in (23)-(25). Again, $\alpha_{R,1}$ and $\beta_{R,1}$ are zero at $\theta_1 = 0, \pi$, while $\alpha_{R,1}$ is always positive. The sign of $\beta_{R,1}$ is now opposite to that of β_1, as confirmed by the direction of the corresponding characteristics – see Fig. 7. Moreover, since $\gamma_{R,1}$ and γ_1 have also opposite signs, equation (27) is now stable on $[\pi/2, 3\pi/2]$, where both $\alpha_{R,1}$ and $\gamma_{R,1}$ are nonnegative. According to the direction of the characteristics, we must now set the boundary condition at $\theta_1 = \pi$.

The initial condition for the time reversed equation (27) is given by the value of u at $t = T$, where T is the final recording or simulation time. Since it is no longer possible to distinguish u_1 from u_2 at later times, we must set the final time T sufficiently large so that the total wave field has left the computational domain and thus vanishes throughout Ω. Hence, we set $f_1 = 0$ at $t = T$, or $f_{R,1} = 0$ at $t = 0$, equivalently.
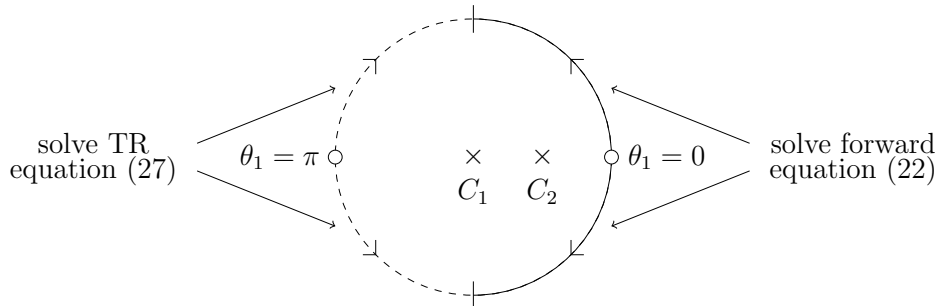
13

Figure 8: The domain of validity for the recovery of f_1 and $f_{R,1}$. Plain line: solve the forward equation (22). Dashed line: solve the time-reversed (TR) equation (27). The characteristics point away from the two small circles at $\theta_1 = 0, \pi$, where the boundary conditions are set, towards the vertical bars at $\theta_1 = -\pi/2, \pi/2$, which mark the end of validity of each quarter-circle.

Finally, we recover u_1 by solving (22) on $[-\pi/2, 0[\bigcup]0, \pi/2]$ forward in time and (27) backward in time on $[\pi/2, \pi[\bigcup]\pi, 3\pi/2]$, as shown in Fig. 8. In pratice, due to the two dividing characteristics at $\theta_1 = 0, \pi$, we actually solve four partial differential equations on four quarter-circles independently of each other. Since (22) and (27) both involve only partial derivatives but no integrals, our approach is local in time and in space. In fact, to reconstruct the signal at any fixed point P at some time $t_0 > 0$, we need to know the total field only on the fraction of the circle from $\theta_1 = 0$ to P, or from $\theta_1 = \pi$ to P, respectively, and for $t \in [0, t_0]$.

Note that in the special case when u_1 or u_2 corresponds to a purely radial wave generated by a point source, the corresponding partial differential equation (22) or (27) reduces to an ordinary differential equation, which can be solved for any particular angle independently, regardless of the shape of Ω.

3.2. Recovery of u_2

In the previous section, we derived equations (22) and (27) to recover u_1 on the entire circle Γ. From the recorded data u, we can thus simply recover u_2 by subtraction. However, we can also recover u_2 from a new independent equation by applying $B_1 := B_1^1$ from (6) instead of B_2 to u:

$$\left(\frac{1}{c} \frac{\partial}{\partial t} + \frac{\partial}{\partial r_1} + \frac{1}{2r_1} \right) u_2 = \left(\frac{1}{c} \frac{\partial}{\partial t} + \frac{\partial}{\partial r_1} + \frac{1}{2r_1} \right) u. \qquad (29)$$
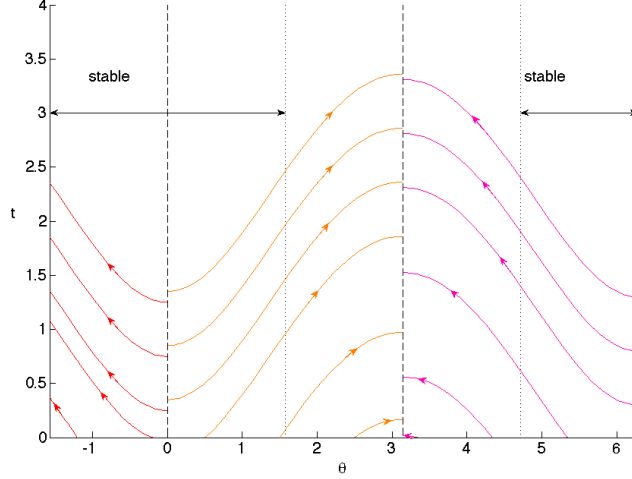
14

Figure 9: Characteristic curves for (31) starting from different angles θ

Again, we use (20) to replace the radial derivative on the left of (29) by a combination of radial and tangential derivatives. Next, we use (7) with $m = 1$ and $k = 2$, that is

$$\frac{\partial}{\partial r_2}(\sqrt{r_2}u_2) = -\frac{1}{c}\frac{\partial}{\partial t}(\sqrt{r_2}u_2), \tag{30}$$

to replace the remaining radial derivative by a time derivative. Thus, we obtain the following partial differential equation for the leading order term $f_2 := f_{2,0}(r_2 - ct, \theta_2)$ in the series expansion (4) of u_2:

$$\left(\alpha_2(\theta_1)\frac{\partial}{\partial t} + \beta_2(\theta_1)\frac{\partial}{\partial \theta_1} + \gamma_2(\theta_1)\right) f_2 = \left(\frac{1}{c}\frac{\partial}{\partial t} + \frac{\partial}{\partial r_1} + \frac{1}{2r_1}\right) u. \tag{31}$$

Here, the coefficient functions are given by

$$\alpha_2(\theta_1) = \frac{\sqrt{r_1^2 + \ell^2 - 2r_1\ell\cos(\theta_1)} - r_1 + \ell\cos(\theta_1)}{c\sqrt[4]{r_1^2 + \ell^2 - 2r_1\ell\cos(\theta_1)}(r_1 - \ell\cos(\theta_1))},$$

$$\beta_2(\theta_1) = \frac{\ell\sin(\theta_1)}{r_1\sqrt[4]{r_1^2 + \ell^2 - 2r_1\ell\cos(\theta_1)}(r_1 - \ell\cos(\theta_1))},$$

$$\gamma_2(\theta_1) = \frac{1}{2\sqrt[4]{r_1^2 + \ell^2 - 2r_1\ell\cos(\theta_1)}(r_1 - \ell\cos(\theta_1))}\left(\frac{\ell\cos(\theta_1)}{r_1} - \frac{\ell^2\sin(\theta_1)^2}{r_1^2 + \ell^2 - 2r_1\ell\cos(\theta_1)}\right).$$

15

Note that α_2, β_2 and γ_2 are still functions of θ_1, since we recover u_2 on the circle Γ still centered at C_1. Remarkably, the signs of α_2, β_2 and γ_2 coincide with those of α_1, β_1 and γ_1, respectively, and so do the characteristics curves – see Fig. 9. Therefore, the same conclusions hold about the initial condition, the boundary conditions at $\theta_1 = 0, \pi$, and the stability properties of (31) on $[-\pi/2, 0) \cup (0, \pi/2]$. Similarly, we use the time reversed counterpart of (31), which is omitted here, to reconstructed u_2 on $[\pi/2, \pi) \cup (\pi, 3\pi/2]$ – see Fig. 8.

3.3. Numerical discretization

To determine u_1 on Γ, we shall solve (22) or (27) numerically, depending on the quarter-circle considered. For the numerical discretization, we opt for the standard Crank-Nicolson scheme in time and upwinding finite differences in space following the characteristics. The numerical discretization of (27) on $\left[\frac{\pi}{2}, \pi\right)$, for instance, reads:

$$
\begin{aligned}
\alpha(i\Delta\theta)\frac{f_i^{n+1} - f_i^n}{\Delta t} \ &+ \ \frac{1}{2}\beta(i\Delta\theta)\left(\frac{f_{i+1}^{n+1} - f_i^{n+1}}{\Delta\theta} + \frac{f_{i+1}^n - f_i^n}{\Delta\theta}\right) \\
&+ \frac{1}{2}\gamma(i\Delta\theta)\left(f_i^{n+1} + f_i^n\right) \ = \ \frac{1}{2}\left(g_i^{n+1} + g_i^n\right),
\end{aligned}
\tag{32}
$$

with $g_i^n = B_{R,2}[u](t^n, i\Delta\theta)$ and $f_1^0 \equiv 0$ at $t = 0$.

To compute the right-hand-side $g_i^n = B_{R,2}[u](t^n, i\Delta\theta)$ in (27), the wave field u and its radial derivative are both computed with the finite element software FreeFem++ [18]. Indeed, from the variational formulation, we easily get an accurate approximation of the radial derivative at Γ, since

$$
\int_\Gamma \frac{\partial u}{\partial r_j} v \ = \ \int_\Gamma \frac{\partial u}{\partial n} v \ = \ \iint_\Omega \frac{\partial^2 u}{\partial t^2} w + \iint_\Omega \nabla u \cdot \nabla w \,.
\tag{33}
$$

Here, Γ denotes a circle centered at C_j, while $w \in H^1(\Omega)$ is an extension of the trace $v \in H^{\frac{1}{2}}(\Gamma)$ into Ω, which vanishes on all vertices inside Ω. For the time and tangential derivatives, we use finite differences and cubic spline interpolation. As the numerical discretizations used on the left and right side of (32) differ, we also avoid any potential "inverse crime".

4. Numerical examples

To illustrate the usefulness of the wave splitting approach described in Section 3, we now consider numerical experiments in two different geometric configurations.

4.1. Two point sources

First, we consider two point sources $F_1(t)$ and $F_2(t)$, located at C_1 and C_2 – see Fig. 1. Each source generates an outgoing wave field u_j. At the outer boundary, we record their sum: $u = u_1 + u_2$. Given that observed data on Γ, we wish to recover the two separate components u_1 and u_2. Hence, u satifies the wave equation

$$\frac{\partial^2 u}{\partial t^2} - c^2 \Delta u \;=\; F_1(t)\delta_{x=C_1} + F_2(t)\delta_{x=C_2}, \quad \text{in } \mathbb{R}^2, \tag{34}$$

with homogeneous initial conditions. The time dependence of the two sources F_1 and F_2, shown in Fig. 10, is given by
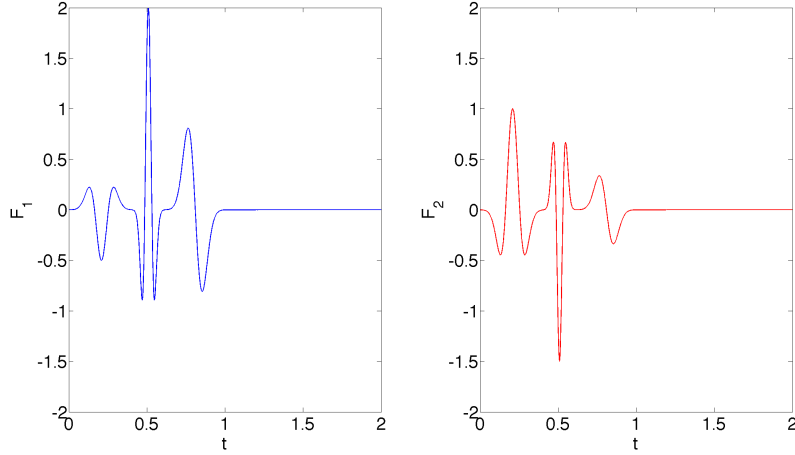

Figure 10: Time dependence of the two point sources F_1 and F_2 in (34).

$$
\begin{aligned}
F_1(t) \;&=\; \left[1 - 2\pi^2(\nu(t-d_1)-1)^2\right] e^{-\pi^2(\nu(t-d_1)-1)^2} \\
&\quad -\frac{3}{2}\left[1 - 2\pi^2(2\nu(t-d_2)-1)^2\right] e^{-\pi^2(2\nu(t-d_2)-1)^2} \\
&\quad -\frac{3}{5}\pi^2(\nu(t-d_3)-1)e^{-\pi^2(\nu(t-d_3)-1)^2},
\end{aligned}
\tag{35}
$$

$$
\begin{aligned}
F_2(t) \;&=\; -\frac{1}{2}\left[1 - 2\pi^2(\nu(t-d_1)-1)^2\right] e^{-\pi^2(\nu(t-d_1)-1)^2} \\
&\quad +2\left[1 - 2\pi^2(2\nu(t-d_2)-1)^2\right] e^{-\pi^2(2\nu(t-d_2)-1)^2} \\
&\quad -\frac{1}{4}\pi^2(\nu(t-d_3)-1)e^{-\pi^2(\nu(t-d_3)-1)^2}
\end{aligned}
\tag{36}
$$

17

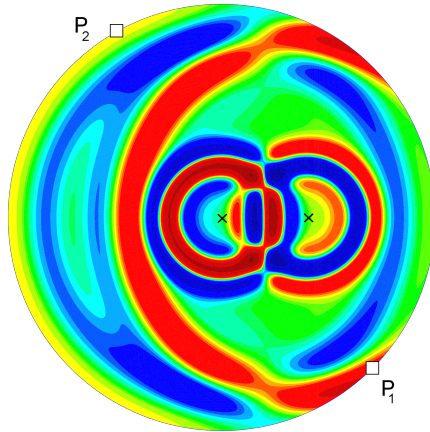Figure 11: Two point sources. Snapshot of the total wave field at $t = 0.64$.

with $d_1 = 0.01$, $d_2 = 0.41$, $d_3 = 0.61$ and $\nu = 5$. They consist of the superposition of three time shifted Ricker-like sources. Next, we set $c \equiv 1$, the wavelength $\lambda = 0.2$ and let C_1 and C_2 equal $(-\lambda/2, 0)$ and $(\lambda/2, 0)$, respectively. The total field is recorded on a circle Γ centered at C_1 with radius $5\lambda/2$ – see Fig. 11.

In Fig. 12, we display the time history of the recovered two wave fields u_1 and u_2 at P_1, located on Γ at $\theta_1 = -\pi/4$. Due to the particularly simple set-up, here both u_1 and u_2 are known explicitly and for all time. In the top left frame, we compare u_1, obtained by solving (22), with the exact wave field and observe that both coincide quite well. Similarly, the wave field u_2, recovered by solving (31), compares favorably with the exact wave field emanating from C_2. Then in the top right frame, we compare the sum $u_1 + u_2$ of the two recovered fields from (22) and (31), with the recorded total field u. Here we observe tiny errors in the reconstruction due to the first-order approximation in the progressive wave expansion (4). Nevertheless, when we add the recovered signals u_1 and u_2 and compare them to the recorded total field, the discrepancy is smaller than 1% of the average amplitude.

In Fig. 13, we show the time history of the recovered fields u_1 and u_2 at P_2 located at $\theta_1 = 3\pi/5$. To recover u_1, we thus solve the time reversed equation (27), and the time reversed counterpart of (31) to obtain u_2. Again, the recovered outgoing wave fields u_1 and u_2 agree remarkably well with the exact wave fields.
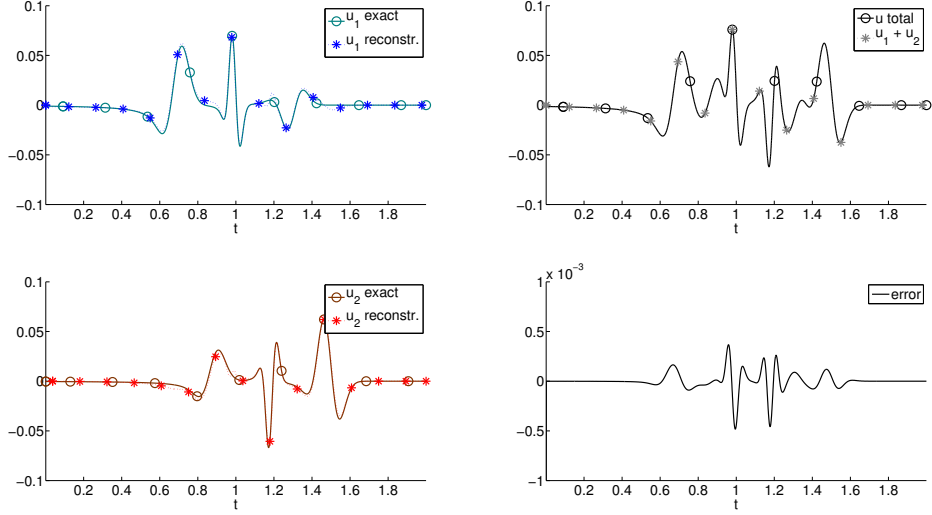
18

Figure 12: Two point sources. Both u_1 and u_2, recovered from total field measurements u, are shown at location P_1 vs. time. Top-left: recovery of u_1 by solving (22). Bottom-left: recovery of u_2 by solving (31). Top-right: total field u. Bottom-right: discrepancy between u and the sum of the recovered fields $u_1 + u_2$.
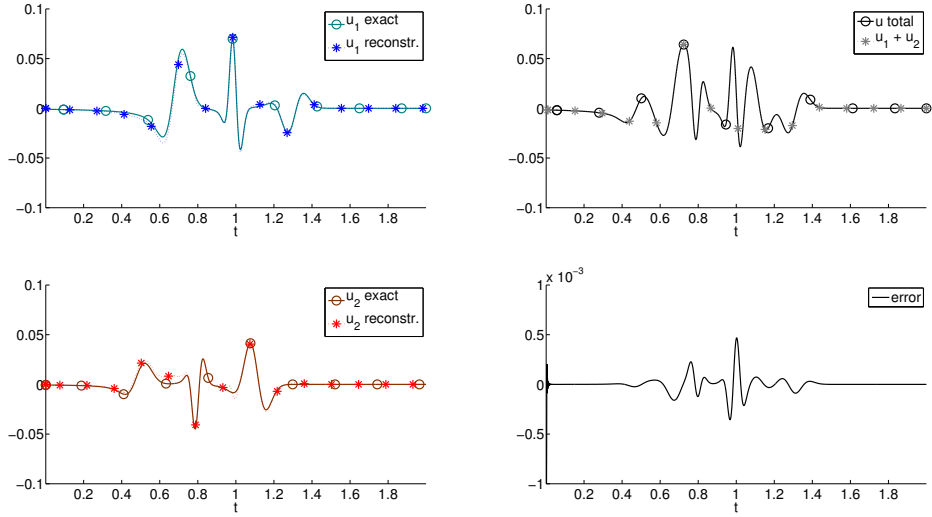

Figure 13: Two point sources. Both u_1 and u_2, recovered from total field measurements u, are shown at location P_2 vs. time. Top-left: recovery of u_1 by solving (27). Bottom-left: recovery of u_2 by solving the time reversed (31). Top-right: total field u. Bottom-right: discrepancy between u and the sum of the recovered fields $u_1 + u_2$.

19

4.2. Scattering from a sound-soft inclusion

Next, we consider scattering from a sound-soft inclusion. Here, the total field consists of the incident wave u^I and the scattered wave u^S. The incident field, generated by the same point source F_1 as in (35), impinges upon a sound-soft fish-shaped obstacle, shown in Fig. 14. It is then scattered into the surrounding medium, where it mingles with the incident field as it reaches the outer circle Γ.
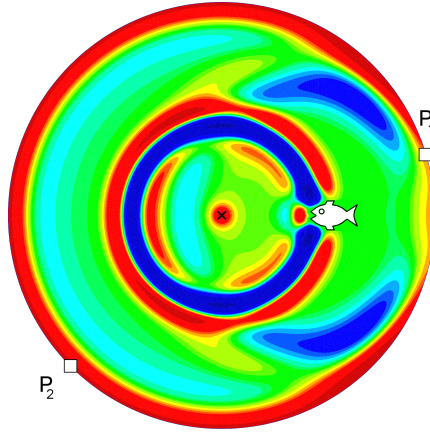

Figure 14: Scattering from a sound-soft inclusion. Snapshot of the total wave field at $t = 0.73$.

Again, we set $\nu = 5$, $c = 1$ and $\lambda = 0.2$. The point source, however, is located at $C_1 = (-3\lambda/4, 0)$ such that the distance between the source and the head of the fish (first impact) is λ. In contrast to the previous case, the scattered field $u_2 = u^S$ is neither purely radial nor explicitly known. Whereas C_1 corresponds precisely to the source location, we set C_2 to $(\lambda/2, 0)$, knowing only approximately the origin of the scattered wave field from the obstacle. Again, the total field u^T is recorded at Γ, the circle of radius $5\lambda/2$ centered at C_1.

In Fig. 15, we display the exact and the recovered wave fields located on Γ at P_1 located at $\theta_1 = \pi/12$. Here, u_1 denotes the incident wave u^I, originating from the point source, and u_2 the scattered field u^S due to the obstacle. In the top left frame, we compare u_1, obtained by solving (22), with the exact wave field and observe that both coincide quite well. Similarly, the wave field u_2, recovered by solving (31), compares favorably with the exact
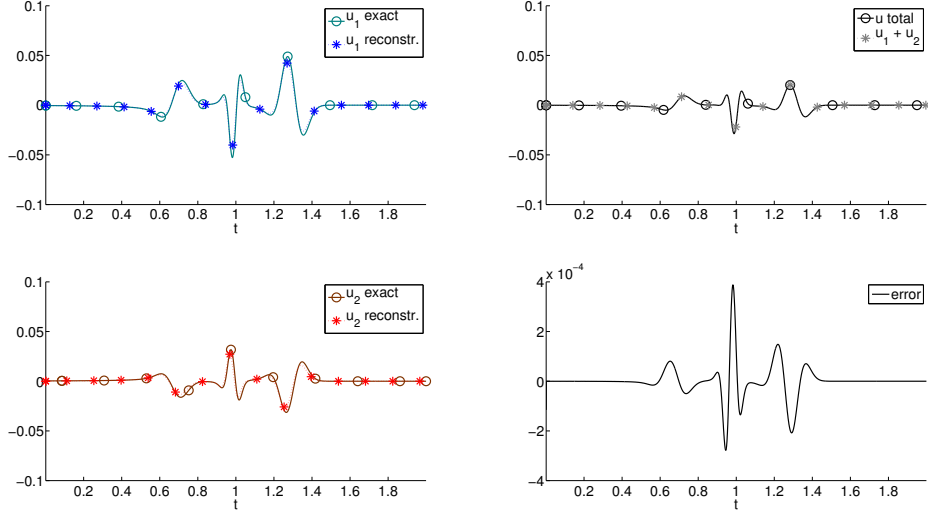
Figure 15: Scattering from a sound-soft inclusion. Both u_1 and u_2, recovered from total field measurements u, are shown at location P_1 vs. time. Top-left: recovery of $u_1 = u^I$ by solving (22). Bottom-left: recovery of $u_2 = u^S$ by solving (31). Top-right: total field $u = u^T$. Bottom-right: discrepancy between u and the sum of the recovered fields $u_1 + u_2$.

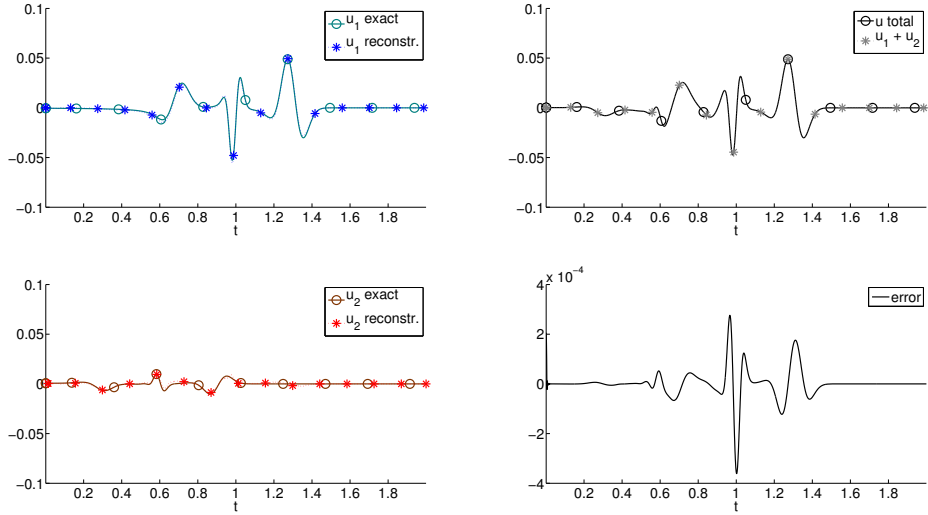Figure 16: Scattering from a sound-soft inclusion. Both u_1 and u_2, recovered from total field measurements u, are shown at location P_2 vs. time. Top-left: recovery of $u_1 = u^I$ by solving (27). Bottom-left: recovery of $u_2 = u^S$ by solving the time reversed (31). Top-right: total field $u = u^T$. Bottom-right: discrepancy between u and the sum of the recovered fields $u_1 + u_2$.

21

wave field emanating from C_2. Then in the top right frame, we compare the sum $u_1 + u_2$ of the two recovered fields from (22) and (31), with the recorded total field u. Here we observe tiny errors in the reconstruction due to the first-order approximation in the progressive wave expansion (4). Nevertheless, when we add the recovered signals u_1 and u_2 and compare them to the recorded total field, the discrepancy is still smaller than 1% of the average amplitude. Although u is small at P_1 due to the wave cancellation inside the shadow zone, we are still able to split it into the incident and scattered field, both larger in magnitude than the observed total field.

In Fig. 16, we show the time history of the recovered fields u_1 and u_2 at P_2 located at $\theta_1 = 5\pi/4$. Here, we solve the time reversed equation (27) to recover u_1, and the time reversed counterpart of (31) to obtain u_2. The observation point P_2 is now closer to the point source at C_1 than to the obstacle. Again, the recovered outgoing wave fields u_1 and u_2 agree remarkably well with the exact wave fields. Although the incident field clearly dominates the scattered field in amplitude, we are still able to recover the time history of both wave fields.

4.3. Noisy observations

Finally, to verify the robustness of our wave splitting approach, we now add multiplicative noise to the observations as follows. Let

$$N(t_j, x_i) := 1 + \sigma \xi_{i,j}, \tag{37}$$

where x_i denotes the position of receiver i, t_j denotes the jth time step, $\xi_{i,j} = \mathcal{N}(0,1)$ is a centered reduced normally distributed random variable, and σ is the noise level. Instead of regularizing the observations prior to differentiation in (22), (31), we directly multiply the right-hand side of (22) as

$$[\alpha(\theta_k)\partial_t + \beta(\theta_k)\partial_{\theta_k} + \gamma(\theta_k)] f_k \; = \; N \times g(u). \tag{38}$$

In Fig. 17, we performed our wave splitting approach on a perturbed right-hand-side in the case of two point sources. We apply 50% Gaussian noise to the right-hand-side as described in (38) and display the exact and the recovered wave fields on Γ for $\theta_1 = 13\pi/12$. Again, the time history of fields u_1 and u_2 is recovered with small perturbations. As before, we also display the sum of the two recovered wave fields and observe that it is also little perturbed – see zoom in Fig. 18. In summary, our wave splitting approach seems remarkably robust with respect to added noise.
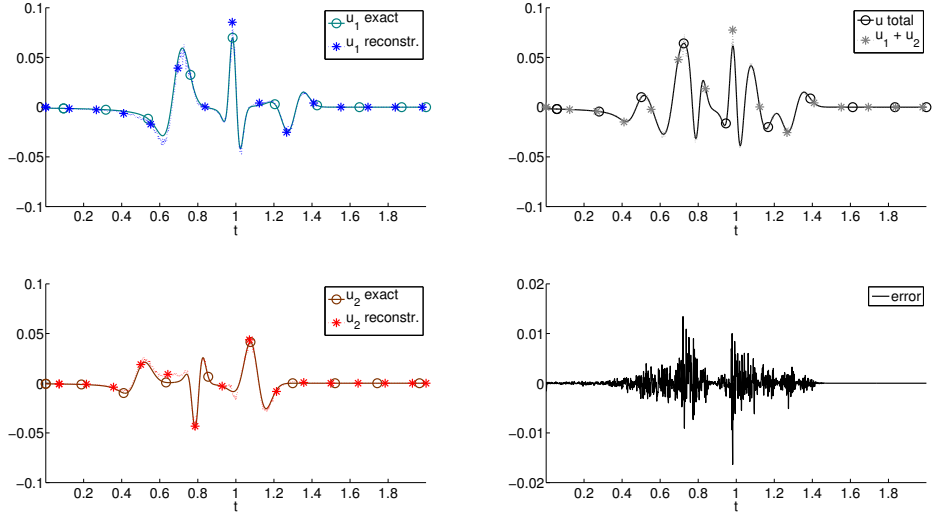
22

Figure 17: Noisy observations. Both u_1 and u_2, recovered from total field measurements u with 50% noise, are shown at location P_2 vs. time. Top-left: recovery of u_1 by solving (27). Bottom-left: recovery of u_2 by solving the time reversed (31). Top-right: total field u. Bottom-right: discrepancy between u and the sum of the recovered fields $u_1 + u_2$.

Figure 18: Noisy observations. Zoom of the recovery of wave fields u_1 and u_2 from total field measurements u with 50% noise, are shown at location P_2 vs. time. Top-left: zoom of the recovery of u_1 by solving (27). Bottom-left: zoom of the recovery of u_2 by solving the time reversed (31). Top-right: total field u. Bottom-right: discrepancy between u and the sum of the recovered fields $u_1 + u_2$.
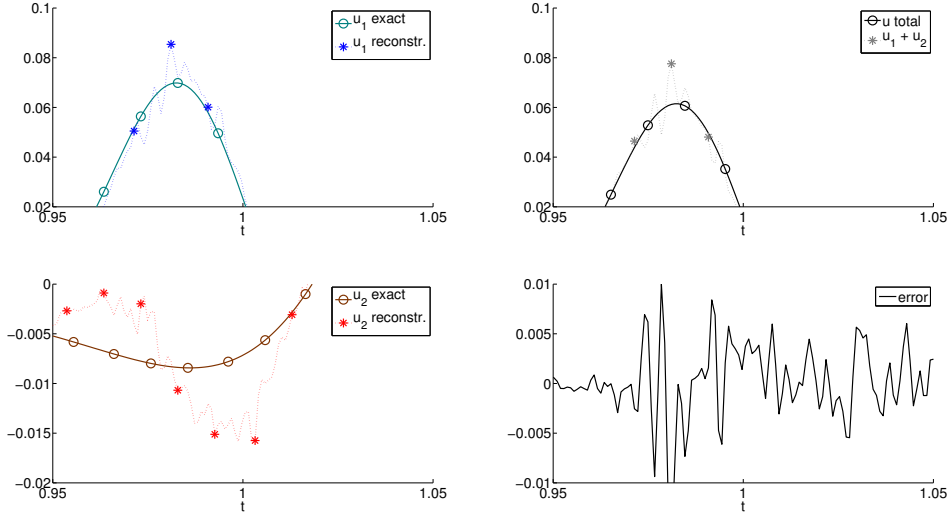
23

5. Concluding remarks

Starting from classical absorbing boundary conditions, we have devised a method to split a time-dependent, scattered, total wave field u into its distinct outgoing components, u_i, induced by separate sources or obstacles. In doing so, we have shown that every u_i satisfies a hyperbolic partial differential equation on the submanifold Γ, where total field measurements are assumed available. Depending on the particular geometry considered, the resulting initial-boundary value problem for u_i on any subset of Γ is well-posed either forward or backward in time. In two space dimensions, for instance, when Γ lies on a circle, it is given by (22), (27) for the scattered field component induced by any source or obstacle at the center of Γ. Since it involves only time or tangential derivatives of u_i at Γ, our approach is truly local in space and time.

The derivation presented here in detail for two space dimensions, immediately extends to three space dimensions. In fact, we then expect even higher accuracy from the first-order Bayliss-Turkel condition (5), because the progressive wave expansion (3) now truly converges at finite distance while higher order corrections decay even faster with distance. Clearly, higher order absorbing boundary conditions, or possibly their counterparts without high-order derivatives [16, 17], could be used for higher accuracy, if needed. In particular, in the presence of three or more obstacles, higher order boundary conditions are probably needed for splitting the scattered fields. Our wave splitting approach also immediately applies to vector-valued wave equations, such as from electromagnetics and elasticity, for which local absorbing boundary conditions are known [19, 11, 24].

Once any scattered field component u_i has been extracted from the total wave field, the corresponding inverse problem can be solved separately to recover the individual scatterer. Thus, the computational domain will be smaller in size and the inverse problem less ill-conditioned than the original multiple scattering inverse problem. Even further reduction of the computational domain can be achieved by back-propagating numerically u_i towards the scatterer using the $TRAC$ method [9], which will also yield an additional noise reduction in the data [4].

When the different components of the total wave field are not due to separate sources or scatterers, yet propagate at different speeds, such as shear and pressure waves in elasticity, our wave splitting approach probably also applies. Thus by applying appropriate radiation boundary conditions [19, 24]

to the total elastic wave field, we could separate shear from pressure wave and thereby improve, for instance, full-field elasticity imaging [3].

Acknowledgements

References

[1] S. Acosta. On-surface radiation condition for multiple scattering of waves. *Comput. Meth. Appl. Mech. Engrg.*, 283:1296–1309, 2015.

[2] R. Aichner, H. Buchner, F. Yan, and W. Kellermann. A real-time blind source separation scheme and its application to reverberant and noisy acoustic environments. *Signal Processing*, 86(8):1260–1277, 2006.

[3] H. Ammari, E. Bretin, J. Garnier, W. Jing, H. Kang, and A. Wahab. Localization, stability, and resolution of topological derivative based imaging functionals in elasticity. *SIAM J. Imaging Sci.*, 6(4):2174–2212, 2013.

[4] F. Assous, M. Kray, F. Nataf, and E. Turkel. Time Reversed Absorbing Condition: Application to inverse problem. *Inverse Problems*, 27(6):065003, 2011.

[5] A. Bayliss and E. Turkel. Radiation boundary conditions for wave-like equations. *Comm. Pure Appl. Math.*, 33(6):707–725, 1980.

[6] A. Belouchrani, K. Abed-Meraim, J.-F. Cardoso, and E. Moulines. A blind source separation technique using second-order statistics. *Signal Processing, IEEE Trans.*, 45(2):434–444, 1997.

[7] F. Ben Hassen, J. Liu, and R. Potthast. On source analysis by wave splitting with applications in inverse scattering of multiple obstacles. *J. Comput. Math*, 25(3):266–281, 2007.

[8] M. Castella, P. Bianchi, A. Chevreuil, and J.-C. Pesquet. A blind source separation framework for detecting CPM sources mixed by a convolutive MIMO filter. *Signal Processing*, 86(8):1950–1967, 2006.

[9] M. de Buhan and M. Kray. A new approach to solve the inverse scattering problem for waves: combining the TRAC and the Adaptive Inversion methods. *Inverse Problems*, 29(8):085009, 2013.

[10] R. Griesmaier, M. Hanke, and J. Sylvester. Far field splitting for the Helmholtz equation. *SIAM J. Numer. Anal.*, 52(1):343–362, 2014.

[11] M. J. Grote. Local nonreflecting boundary condition for Maxwell's equations. *Comput. Meth. Appl. Mech. Engrg.*, 195(29-32):3691–3708, 2006.

[12] M. J. Grote and C. Kirsch. Dirichlet-to-Neumann boundary conditions for multiple scattering problems. *J. Comput. Phys.*, 201(2):630–650, 2004.

[13] M. J. Grote and C. Kirsch. Nonreflecting boundary condition for time-dependent multiple scattering. *J. Comput. Phys.*, 221(1):41–67, 2007.

[14] M. J. Grote, M. Kray, F. Nataf, and F. Assous. Wave splitting for time-dependent scattered field separation. *Comptes Rendus Mathematiques*, 353(6):523–527, 2015.

[15] M. J. Grote and I. Sim. Local nonreflecting boundary condition for time-dependent multiple scattering. *J. Comput. Phys.*, 230(8):3135–3154, 2011.

[16] T. Hagstrom and S. I. Hariharan. A formulation of asymptotic and exact boundary conditions using local operators. *Applied Numerical Mathematics*, 27:403–416, 1998.

[17] T. Hagstrom and T. Warburton. A new auxiliary variable formulation of high-order local radiation boundary conditions: corner compatibility conditions and extensions to first-order systems. *Wave Motion*, 39(4):327–338, 2004.

[18] F. Hecht. New development in FreeFem++. *J. Numer. Math.*, 20(3-4):251–265, 2012.

[19] R. L. Higdon. Radiation boundary conditions for elastic wave propagation. *SIAM J. Numer. Anal.*, 27(4):831869, 1990.

[20] A. L. Klibanov, P. T. Rasche, M. S. Hughes, J. K. Wojdyla, K. P. Galen, J. H. J. Wible, and G. H. Brandenburger. Detection of Individual Microbubbles of Ultrasound Contrast Agents: Imaging of Free-Floating and Targeted Bubbles. *Investigative Radiology*, 39(3):187–195, 2004.

[21] K. L. Kreider. A wave splitting approach to time dependent inverse scattering for the stratified cylinder. *SIAM J. Appl. Math.*, 49(3):932–943, 1989.

[22] M. Pernot, G. Montaldo, M. Tanter, and M. Fink. Ultrasonic stars for time reversal focusing using induced cavitation bubbles. *Appl. Phys. Lett.*, 88(3):034102, 2006.

[23] R. Potthast, F. M. Fazi, and P. A. Nelson. Source splitting via the point source method. *Inverse Problems*, 26(4):045002, 2010.

[24] D. Rabinovich, D. Givoli, J. Bielak, and T. Hagstrom. A finite element scheme with a high order absorbing boundary condition for elastodynamics. *Comput. Methods Appl. Mech. Engrg.*, 200(23-24):2048–2066, 2011.

[25] T. Saratoon, T. Tarvainen, B. T. Cox, and S. R. Arridge. A gradient-based method for quantitative photoacoustic tomography using the radiative transfer equation. *Inverse Problems*, 29(7):075006, 19, 2013.

[26] V. Twersky. On multiple scattering of waves. *J. Res. Nat. Bur. Standards*, 64D:715–730, 1960.

[27] V. H. Weston. Factorization of the wave equation in higher dimensions. *J. Math. Phys.*, 28:1061–1068, 1987.

LATEST PREPRINTS

No.	**Author:** *Title*

2015-11   **G. Crippa, N. Gusev, S. Spirito, E. Wiedemann**
Non-Uniqueness and Prescribed Energy for the Continuity Equation

2015-12   **G. Crippa, S. Spirito**
Renormalized Solutions of the 2D Euler Equations

2015-13   **G. Crippa, E. Semenova, S. Spirito**
Strong Continuity for the 2D Euler Equations

2015-14   **J. Diaz, M. J. Grote**
Multi-Level Explicit Local Time-Stepping Methods for Second-Order Wave Equations

2015-15   **F. Da Lio, L. Martinazzi, T. Riviere**
Blow-up analysis of a nonlocal Liouville-type equation

2015-16   **A. Maalaoui, L. Martinazzi, A. Schikorra**
Blow-up behaviour of a fractional Adams-Moser-Trudinger type inequality in odd dimension

2015-17   **T. Boulenger, E. Lenzmann**
Blowup for Biharmonic NLS

2015-18   **D. Masser, U. Zannier (with Appendix by V. Flynn)**
Torsion point on families of simple abelian surfaces and Pell's equation over polynomial rings

2015-19   **M. Bugeanu, R. Di Remigio, K. Mozgawa, S. S. Reine, H. Harbrecht, L. Frediani**
Wavelet Formulation of the Polarizable Continuum Model. II. Use of Piecewise Bilinear Boundary Elements

2015-20   **J. Dölz, H. Harbrecht, M. Peters**
An interpolation-based fast multipole method for higher order boundary elements on parametric surfaces

2015-21   **A. Schikorra**
Nonlinear Comutators for the fractional p-Laplacian and applications

2015-22   **L. Martinazzi**
Fractional Adams-Moser-Trudinger type inequalities

Preprints are available under *https://math.unibas.ch/research/publications*

LATEST PREPRINTS

No.	**Author:** *Title*

2015-23   **P. Habegger, J. Pila**
O-Minimality and certain atypical intersections

2015-24   **P. Habegger**
Singular Moduli that are Algebraic Units

2015-25   **P. Habegger, F. Pazuki**
Bad Reduction of genus 2 curves with CM jacobian varieties

2015-26   **A. Bohun, F. Bouchut, G. Crippa**
Lagrangian solutions to the 2D Euler system with L^1 vorticity and infinite energy

2015-27   **A.-L. Haji-Ali, H. Harbrecht, M. Peters, M. Siebenmorgen**
Novel results for the anisotropic sparse quadrature and their impact on random diffusion problems

2015-28   **P. Habegger, G. Jones, D. Masser**
Six unlikely intersection problems in search of effectivity

2015-29   **M. Griebel, H. Harbrecht, M. Peters**
Multilevel quadrature for elliptic parametric partial differential equations on non-nested meshes

2015-30   **M. J. Grote, M. Kray, F. Nataf, F. Assous**
Time-dependent wave splitting and source separation

Preprints are available under *https://math.unibas.ch/research/publications*